EPJ Photovoltaics **16**, 2 (2025)

https://doi.org/10.1051/epjpv/2024042

Available online at:
www.epj-pv.org

Special Issue on 'EU PVSEC 2024: State of the Art and Developments in Photovoltaics', edited by Robert Kenny and Gabriele Eder

ORIGINAL ARTICLE OPEN ACCESS

An investigation on the uncertainty of fill factor

Diego Pavanello*, Tony Sample, and Harald Müllejans

European Commission, Joint Research Centre, Ispra, Italy

Received: 28 June 2024 / Accepted: 28 November 2024

Abstract. This study focuses on the fill factor (*FF*) measurement uncertainty contributing to the uncertainty in the labeling of the nominal maximum power (P_{max}) of photovoltaic modules, which is determined under Standard Test Conditions (STC). Given that the price of these modules is tied to their P_{max}, accurately quantifying the uncertainty of this measurement is crucial for ISO/IEC 17025 accredited laboratories. Adhering to the "Guide to the expression of uncertainty in measurement", this work evaluates the uncertainty contribution of the Fill Factor (*FF*), a key parameter linking P_{max}, the open-circuit voltage (V_{oc}), and the short-circuit current (I_{sc}). The analysis is based on data from three reference modules measured at the European Solar Test Installation (ESTI), part of the Joint Research Centre of the European Commission, since 1996. This data shows a reduction in *FF* uncertainty from approximately 0.6% to 0.3%, attributed to advancements in measurement technologies and techniques. Considering the goal of top calibration laboratories to measure P_{max} with the lowest possible uncertainty, the improvement in *FF* uncertainty measurement is significant, ensuring more accurate labeling of photovoltaic modules.

Keywords: Fill factor / photovoltaic module nominal power / measurement uncertainty

1 Introduction

Photovoltaics (PV) is the technology that converts light directly into electricity. The sun being the most abundant energy source reaching the Earth's surface, PV is the most promising renewable energy at disposal of mankind to reduce the carbon footprint and gas emissions into the atmosphere. Over the last decade, it has become a mature technology, reaching the milestone of 1 TW (Terawatt) installed capacity in 2022, and a realistic forecast for the annual production of PV modules to reach 1 TW within the next 5–7 years [1]. With a quasi-exponential growth foreseen for the upcoming years, such an industry requires and deploys huge financial means, both in terms of large plants and a large number of small and residential PV systems. The cost share of the PV modules with respect to the total cost of a plant has dramatically decreased over the last years, due to cost reduction of the crystalline silicon material, covering about 95% of the PV market [2,3]. The remaining 5% is divided among a variegate population of thin-film materials, in particular CdTe (Cadmium Telluride), CIGS (Copper Indium Gallium Selenide) with several variations (CIGSS), DSSC (dye-sensitized cells), organic devices, multi-junction devices, and the fast-emerging family of perovskites, with record efficiencies above 34% [4].

Independent of the technology, the price of a PV module depends on its nominal maximum power (P_{max}). At the end of the production line, the factory measures the electrical performance of all the modules using solar simulators [5,6], with typical factory uncertainties close to ±3% for P_{max}, due to the differences between the factory measurement conditions and the Standard Test Conditions (STC). The STC conditions are defined as 1000 W/m^2 incident irradiance, 25 °C module temperature and AM1.5 spectrum [7,8]. To perform this task, manufacturers rely on reference devices measured by commercial laboratories with a testing ISO/IEC 17025 accreditation, that in turn rely on the traceability chain provided by several top-level calibration laboratories. The latter have reduced their measurement uncertainties reaching values of 1.0% to 1.5% for P_{max} of crystalline silicon modules, by improving their measurement methods, instrumentation, and analysis of the different factors influencing the overall uncertainty budget.

The most widely used method to determine the measurement uncertainties is described in the "Guide to the expression of uncertainty in measurement" [9], published by BIPM as a practical procedure to calculate the uncertainty of a result if the uncertainties of the input variables and the mathematical model are known.

* e-mail: diego.pavanello@ec.europa.eu

The electrical power is defined as

$$P = VI \tag{1}$$

with P the power, V the voltage and I the current; the uncertainty of maximum power is therefore the value of the uncertainty of a single point of the power curve, and applying the definition in equation (1) would need the knowledge of the uncertainty of all the points of the I–V curve of the module. The common approach is expressing the maximum power in its dimensionless form, the fill factor:

$$FF = \frac{P_{max}}{V_{oc} I_{sc}} \tag{2}$$

from which

$$P_{\max} = V_{oc} I_{sc} FF. \tag{3}$$

Scientific literature offers an extensive knowledge of the uncertainties of I_{sc} and V_{oc}: the short-circuit current is more sensitive to the incident irradiance non-uniformity and the spectrum, while the V_{oc} depends strongly on device temperature. However, they are not sufficient and the contribution of FF cannot be neglected. The present work analyses this component as a "Type A" uncertainty, therefore directly computed from measured data. Three crystalline silicon PV modules have been measured at ESTI at regular intervals since 1996, on solar simulators of different types and technology generations. The dataset of their I–V curves is used to calculate the FF evolution during time, to deepen the understanding of its statistical behavior and assess its impact on the overall $P_{\max}$ uncertainty.

2 Experimental implementation

2.1 Repeatability measurements

The present work is based on a long time-series of I–V curve measurements on three reference modules on different solar simulators at the ESTI laboratories. The purpose of performing such a series is to monitor the stability of the whole measurement chain on a continuous basis in the same conditions (repeatability measurements). The three reference modules are named in the present study ADX00, GC01 and ZZ71 (to keep them anonymous their lab codes are maintained in the text), as listed in Table 1. The first two are smaller than the third, which was added in 2015 due to the tendency of the market to increase the module size, and to the larger measurement area available on the solar simulators. The three modules have no bypass diodes.

In this study, measurements were conducted over the years using various generations of solar simulators and measurement set-ups. Notably, flash systems saw a pulse duration increase from around 2 milliseconds to over 10 milliseconds, with faster optoelectronic feedback systems for better irradiance stabilization during the pulse and enhanced optics to lower spatial non-uniformity of irradiance in the measurement plane. Since 2013, ESTI has also utilized a steady-state large area solar simulator model (Apollo), enabling single I–V measurements with durations (typically 1 second) previously unattainable via flash based simulators (see Tabs. 2 and 3). The uniformity of irradiance of solar simulators is measured according to IEC 60904-9 [5] and regularly checked in the framework of the accreditation requirements. All the simulators used in this paper are classified as class "A" or "A+" on spatial non-uniformity.

Table 1. Overview of the three modules whose repeatability series is used in the present study. The first two (ADX00 and GC01) have been used since 1996 and their size is smaller, while ZZ71 was added several years later.

Module	N. cells	Area (m^2)	Cell type
ADX00	33	0.40	Mono-Si
GC01	36	0.45	Poly-Si
ZZ71	72	1.40	Mono-Si

The electronics, data acquisition components and software are customized in order to be more flexible. The irradiance is measured simultaneously with the electrical output of the module by means of a calibrated reference cell, which is kept dynamically in short-circuit by a trans-impedance amplifier. The device under test (DUT) is loaded with a voltage waveform (typically an increasing linear ramp) from a slightly negative voltage to above the V_{oc} of the module. The current is calculated converting the voltage drop across a calibrated high precision shunt. The data acquisition system is either composed by three voltmeters for steady-state systems or a storage oscilloscope for pulsed simulators. All the instruments are traceably calibrated internally according to ISO/IEC 17025 accredited methods.

All the I–V curves analysed in this study have been acquired setting the irradiance level as close as possible to $1000\,\mathrm{W/m^2}$ and in the temperature range $(25.0 \pm 0.1)\,^{\circ}\mathrm{C}$, in order to minimize the error due to the I–V translation from the measurement conditions to the target conditions (STC without spectral correction) following [10]:

$$I_2 = I_1 + \frac{G_1'}{G_{sc1}} I_{sc1} \left(\frac{G_2}{G_1} - 1 \right) + \alpha (T_2 - T_1) \tag{4}$$

$$V_2 = V_1 - R_s (I_2 - I_1) - \kappa I_2 (T_2 - T_1) + \beta (T_2 - T_1) \tag{5}$$

with the subscript "2" refers to the target conditions, the subscript "1" the measurement conditions, α and β the temperature coefficients of I_{sc} and V_{oc} respectively, T the temperature, R_s the series resistance calculated with [10] and κ the curve correction factor. The term G_{sc1} is the irradiance value at the time of I_{sc1} measurement and G_1' is the irradiance measured at time of data acquisition of individual I–V points. By respecting the above mentioned temperature range of $\pm 0.1\,^{\circ}\mathrm{C}$, the terms involving $(T_2 - T_1)$ can be neglected, and by measuring very close to $1000\,\mathrm{W/m^2}$ the term $R_s(I_2 - I_1)$ can be omitted. The

Table 2. Timeframes of the measurements of the three modules on the different solar simulators since 1996.

Simulator ▶ Module ▼	Spectrolab LAPSS	Pasan 2	Pasan 3B	Apollo
ADX00	1996 – 2011	1996 – 2011	2011 – ongoing	2015 – ongoing
GC01	1996 – 2011	1996 – 2011	2011 – ongoing	2015 – ongoing
ZZ71	N.A.	N.A.	2015 – ongoing	2015 – ongoing

Table 3. List of solar simulators used for the I–V measurements in the present study.

Spectrolab	Pulsed solar simulator with 2 ms pulse duration. Dismissed in 2011.
Pasan 2	Pulsed solar simulator with 20 ms decaying pulse; since 2011 it is not used for I–V measurements.
Pasan 3B	Pulsed solar simulator with 10 ms stabilized pulse; active at ESTI since 2011.
Apollo	Large area steady-state solar simulator (2 m x 2 m illuminated area); active at ESTI since 2013.

translation is therefore reduced to

$$I_2 = I_1 + \frac{G_1^{'}}{G_{sc1}} I_{sc1} \left(\frac{G_2}{G_1} - 1 \right) \tag{6}$$

$$V_2 = V_1 \tag{7}$$

and the knowledge of the coefficients R_s, κ, α and β is not necessary. The point I_{sc1} cannot be directly measured, and is calculated as the intersection of a linear least square fit with the current axis. Using the corrected data set (V_2, I_2) the relevant electrical parameters of the I–V curve can be extracted:

- The short circuit current I_{sc2} is the intersection between the vertical axis and the linear least square fit of the points I_2 with $|V_2| \to 0$.
- The open-circuit voltage V_{oc2} is the intersection between the horizontal axis and the linear least square fit of the points V_2 with $|I_2| \to 0$.
- The maximum power point $P_{\max 2}$ is the absolute maximum of the fourth order polynomial fit of those points in an interval including the point $max(V_2\ I_2)$. The point is calculated analytically imposing the null first derivative of the polynomial. The abscissa V_{mp2} is calculated interpolating the position of the $P_{\max 2}$ point on the voltage array; I_{mp2} is calculated once the other two are known.
- The fill factor is calculated using equation (2).

For the purpose of the repeatability assessment, the calibration value of each reference cell is kept unchanged throughout the entire measurement series over the years, neglecting its yearly change due to successive recalibrations. The stability is anyway verified, with year-to-year variations around 0.2% to 0.3% and no drift in the long term history. For the current study this is actually less important, as a small variation of the reference cell calibration value would change I_{sc} and $P_{\max}$ similarly (same direction and same relative change) such that the FF (Eq. (2)) remains unaffected. On the other hand this is important for the repeatability of I_{sc} and $P_{\max}$ values, which are also monitored at ESTI but not discussed further in this paper.

2.2 Elements of the uncertainty analysis

A correct estimation of the uncertainty associated to $P_{\max}$ of a PV module requires, as already mentioned, prior knowledge of the uncertainties of its terms I_{sc}, V_{oc} and FF. The latter is the subject of the present work, aiming at deepening the knowledge of this component which can be dealt only as a "Type A" contribution.

The GUM [9] offers a worldwide accepted methodology to evaluate the measurement uncertainties; the contributions of the factors having an influence on the output quantity of interest are divided in two types, named "A" and "B". Uncertainties of type "A" can be estimated only by a statistical analysis of measured data, while those of type "B" can be inferred by other means, for example calibration certificates, technical documentation, proven experience, literature and so on.

The subsequent section outlines the primary factors influencing the total uncertainty of $P_{\max}$ (without delving into excessive detail) with the purpose to contextualize the FF contribution with respect to others. It is essential to emphasize that variations in measurement conditions, such as temperature or irradiance alterations, or alterations to the measurement protocol, affect the uncertainty. Thus, a new calculation is required for each method and each instance. The following section refers to the case of measurements at 1000 W/m^2 and 25 °C taken on crystalline silicon modules on one of the pulsed solar simulators used in the present study.

2.3 Electrical uncertainties

The electrical uncertainties arise from the data acquisition system, the current-voltage converter, and the transimpedance amplifier. The data acquisition system can be a

fast oscilloscope or a set of voltmeters, depending on the required data sampling rate. Different channels or measurement ranges of the instrument have in general different uncertainties, however it can be dealt with as a Type B contribution with typical $UC_{DAS} = \pm 0.10\%$ ($k = 2$ or 3). The current-voltage converter is a calibrated high-precision shunt with low-temperature coefficient. Depending on the maximum I_{sc} expected from the devices under test, different shunts are needed to generate sufficient voltage drops across them for an appropriate measurement. This contribution affects only the I_{sc} uncertainty for an amount of $UC_{SH} = \pm 0.12\%$ ($k = 2$). The third element is the device to convert the output signal of the reference cell (typically around 120 mA to 150 mA at 1000 W/m^2) into a voltage signal. Although some models of reference cells are equipped with an internal shunt, for precise measurements an external trans-impedance amplifier is preferable. Passing through the mathematical translation of the curve, the contribution of the irradiance affects both voltage and current for a typical amount of $UC_{TIA} = \pm 0.12\%$ ($k = 2$), as the trans-impedance is amplifier calibrated with the same protocol as the other shunts. It has a major impact on current and less on voltage.

2.4 Temperature uncertainties

The primary sources of uncertainty for temperature measurement include sensor uncertainty, measurement range, and non-uniformity in the device being tested. The sensor and reader function as a combined unit and are calibrated together; each sensor is linked to its specific reader or channel, and any change requires recalibration. The second factor concerns the prescribed measurement conditions in each laboratory method. In repeatability measurements, across all systems, a fixed range of (25.0 ± 0.1) °C is utilized for the device under test (T_{DUT}), which simplifies the translation equations as illustrated above, but introduces a contribution proportional to $\alpha(T\text{-}25)$ for current and $\beta(T\text{-}25)$ for voltage. Lastly, temperature non-uniformity is applicable only for full-size modules; in the case of reference cells, it is disregarded due to two factors: the small device area and the prevalence of active control systems like Peltier elements or water-cooled plates for such devices. Overall, the temperature contribution is in the order of $UC_T = \pm 0.2\%$ ($k = 2$) for V_{oc} of full size modules and much less for the current.

2.5 Optical uncertainties

The most important contributions for full size modules are the spatial non-uniformity of the irradiance in the plane and the spectral correction; other sources are due to the geometrical misalignment of the DUT respect to the reference cell and the calibration of the reference cell itself. Periodic evaluation of irradiance non-uniformity on the plane is conducted using the standard [5] across the entire illuminated area, even though the module under test's active area remains smaller than the total area. The non-uniformity value supplied by the standard is grounded in minimum and maximum irradiance values on the plane, not the dispersion of irradiance values on the map. As a result, the estimated non-uniformity represents the highest potential value. For the solar simulators considered in this study, representative values are between $\pm 0.65\%$ to $\pm 1.1\%$ ($k = 2$) depending on the simulator, for the entire illuminated area. The uncertainty of the spectral mismatch factor [8,11] depends not only on the I–V measurement (simulator spectrum and reference cell spectral responsivity), but also on the spectral responsivity of the module. An indicative value is around $\pm 0.36\%$ ($k = 2$), only applicable to the current. The third relevant optical contribution is the calibration value of the reference cell, stated in its calibration certificate. At ESTI, the set of five primary reference cells have a long history of calibrations with primary methods against absolute cavity radiometers, leading to uncertainties as low as $\pm 0.22\%$ ($k = 2$), while the secondary cells (used to characterize large area modules) have uncertainties of $\pm 0.46\%$ ($k = 2$) in the best case.

2.6 Fill factor

The uncertainty of FF is an item "per se". In literature it is attributed to the cabling and connections of the device under test [12–14]. Its random behavior makes this contribution treated as a type "A" uncertainty, estimated through measured data series. The FF influences the uncertainty of P_{max}. As depicted in Figure 1A, this factor plays a substantial role in the overall uncertainty of P_{max}; however, it cannot be analytically calculated due to its purely stochastic nature. Figures 1B and 1C present the expanded diagrams of the components contributing to I_{sc} and V_{oc} uncertainties. For I_{sc}, irradiance-related terms (reference cell and optical) are predominant, whereas the temperature term is the most influential for V_{oc}. The case depicted in Figure 1 is given as a representative example for ESTI; the individual contributions vary depending on the specific technology and measurement conditions, but their relative distribution on the cake remains valid in general.

3 Results

3.1 Data cleaning

The uncertainty of the FF has been evaluated as a Type "A" contribution using the data series of three crystalline silicon modules, named ADX00, GC01 and ZZ71, whose characteristics have been described above. Their measurements began in 1996 for the first two, while ZZ71 was introduced in 2015. From the entire data set, encompassing about 5200 I–V curves, those acquired indoor at 1000 W/m^2 irradiance and 25 °C module temperature have been extracted, reducing it to 4353 curves. More in detail, the curves were acquired on 4 different solar simulators, by 23 users, throughout 28 years; device ADX00 is represented by 1889 curves, GC01 by 1895, and ZZ71 by 569. Respect to the distribution during the timeline, 218 were taken between 1996 and 2000, 1851 between 2000 and 2010, and 2284 after 2010.

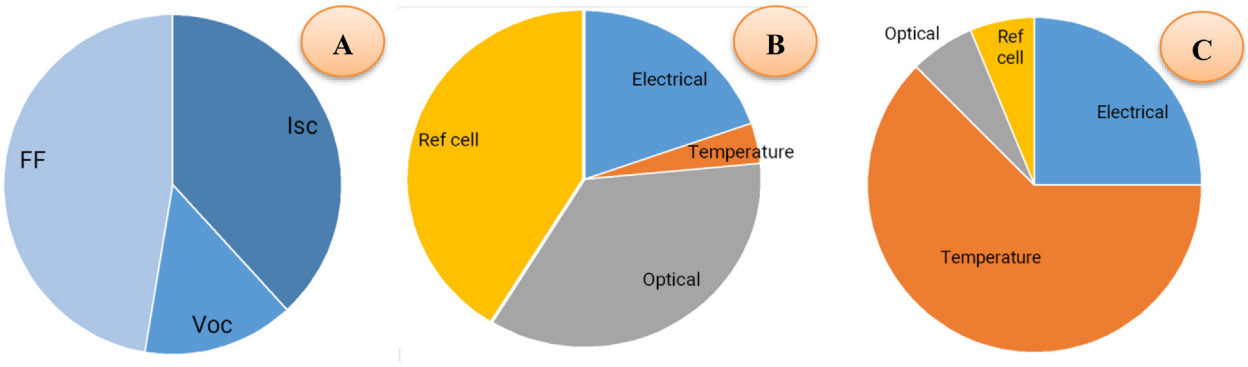

Fig. 1. Contributions to the final uncertainty of $P_{\max}$ for a typical indoor measurement at 1000 W/m^2 and 25 °C. (A): share of the three terms constituting the $P_{\max}$ uncertainty; (B): exploded diagram with the I_{sc} components; (C): exploded diagram with the V_{oc} components.

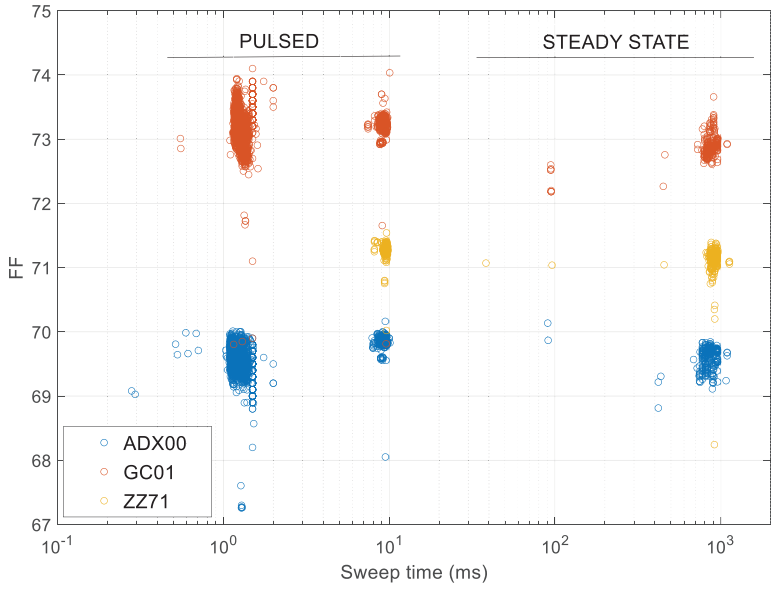

Fig. 2. Fill factor of the three modules at varying sweep times (in milliseconds). Measurements at 10 ms and below were obtained using pulsed solar simulators, while those exceeding 100 ms (up to 1 second) were conducted on the Apollo (steady-state large area) simulator.

Each module has been analyzed individually, dividing the whole dataset into three distinct smaller sets, one for each device. Each measurement of the set has been filtered according the following criteria:
– DUT temperature between 24.5 °C and 25.5 °C;
– Mean irradiance during the I–V sweep between 950 W/m^2 and 1050 W/m^2;
– Target irradiance of 1000 W/m^2;
– Individual z-score of the fill factor between −3 and +3.

The temperature range applied in the filtering process is larger than the range specified in 2.1 to filter out the outliers; in the non-filtered data set also several measurements acquired in custom conditions were present, or for purposes different from the repeatability checks. The filtering process aims at removing these data from the cleaned set.

The z-score of the point FF_i has been calculated with

$$z_i = \frac{FF_i - \mu}{\sigma} \tag{8}$$

with the mean value μ and the standard deviation σ calculated on the entire set of a specific module.

The z-score is a statistical measurement that represents the number of standard deviations an individual data point is from the mean of a dataset. The z-score is used to detect outliers in a dataset because it provides a standardized measure of how far a data point is from the mean in terms of the standard deviation. Outliers are typically defined as data points that are significantly far from the mean, and the z-score helps quantify this distance.

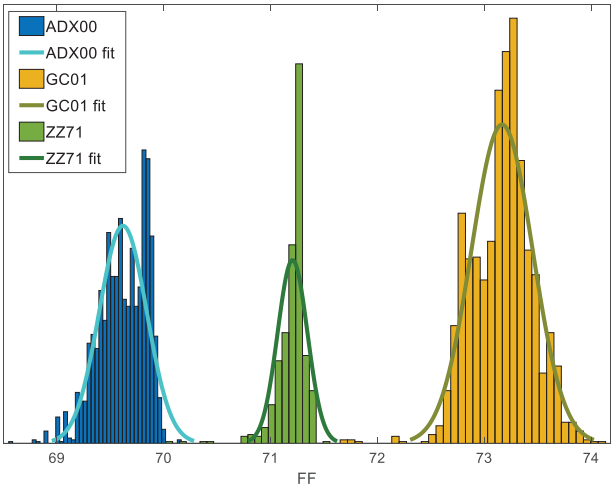

Fig. 3. Histograms of the three datasets with their respective Gaussian distributions.

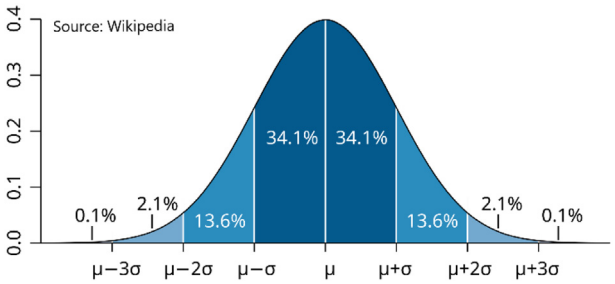

Fig. 4. Confidence intervals applicable to fill factor uncertainty estimation.

When a data point has a z-score that is too high or too low (usually greater than 3 or less than −3), it can be considered an outlier. This threshold is based on the empirical rule, which states that approximately 99.7% of data points fall within three standard deviations of the mean (for a Gaussian distribution). Therefore, any data point with a z-score outside this range is considered an outlier, as it is highly unusual and falls far from the majority of the data.

The dependency of *FF* on measurement speed, or "sweep time", has been evaluated to rule out the possibility of capacitive effect interference in the analysis. It is well known from literature [15] that certain technologies, like highly doped silicon devices and hetero-junction devices, require longer measurement times than those provided by pulsed solar simulators. Capacitive modules necessitate alternative methods like the multi-flash technique or a sufficiently long light source, such as a steady-state simulator, for accurate measurement.

The following Figure 2 shows the *FF* series of all the three modules for varying sweep time; the points with shorter sweep times (up to 10 ms) were taken on the pulsed simulators, while longer sweep times (up to 1 s) on the steady-state large area Apollo simulator. The cross-correlation coefficient **ρ** between the fill factor and the sweep time have been analyzed for all the measurements (from a few milliseconds to about one second). For ADX00 and GC01 it is $\rho = 0.02$ and $\rho = 0.10$ respectively, while for ZZ71 $\rho = 0.30$. For the smaller devices there is no correlation, while for the large area device there is a poor correlation, which might be due to the temperature non-uniformity on the device surface and the small temperature increase during the measurement itself. As a general approach, two quantities are considered correlated for $\rho > 0.7$, although each case needs an ad-hoc evaluation.

3.2 Stochastic behavior of fill factor

The fill factor is a function of three quantities: I_{sc}, V_{oc} and $P_{\max}$. The factors contributing to the uncertainty of I_{sc} and V_{oc} are well known. The variability of the measured fill factor is attributed mainly to the electrical contacting of the PV device with the measurement system. As a standard procedure, the PV module is equipped with its own contacting system, which has to be interfaced with the measurement system in order to make a four-wire connection. Many factors may influence an electrical contact, notably the contact geometry, the roughness, oxidation, corrosion, temperature and humidity of the environment, and wearing of the connectors of both the module and the measurement system. Therefore, in absence of a mathematical model correlating these inputs to the fill factor variation, it is dealt as a type "A" uncertainty to be estimated by statistical analysis.

Other practical elements may affect the distributions of fill factor, for example measurements done by the different simulators and operators in different periods of time. The *FF* probability distribution functions (pdf) across the entire history of the three modules have been computed. From the sample distributions, once verified their Gaussian behavior, the population distributions have been computed by a Gaussian fit model; they are shown in Figure 3, which embraces the entire dataset prior to any filtering. The resolution of the histograms shown in the figure depends on the number of bins, and therefore on the number of points. There is not a fixed rule, as it can vary based on the context and the purpose of the analysis. For the present study, the number of bins is between the number given by the Sturges' rule ($b = \log_2(N) + 1$) and the square root rule ($b = \sqrt{N}$). The former tends to underestimate the number of bins and may be a better choice for smaller samples, while the latter tends to overestimate unless the sample is very large. Figure 3 demonstrates that the *FF* can be practically dealt with as a Gaussian distribution for the purpose of uncertainty estimation for the $P_{\max}$. Independently on the value of the average, the standard deviation **σ** gives the estimate of the uncertainty of *FF*. This means for any single measurement made, we expect the *FF* to deviate from the true value within a Gaussian distribution, with its width described by the standard deviation observed in the sample. This is different from the uncertainty of the *FF* determined for any of the three modules as the mean of the sample. The latter has an uncertainty of the standard deviation divided by the square root of the sample size. But this is not the aim of our determination. The analysis here aims at the determination of typical standard deviations for *FF* as observed on three typical modules and then

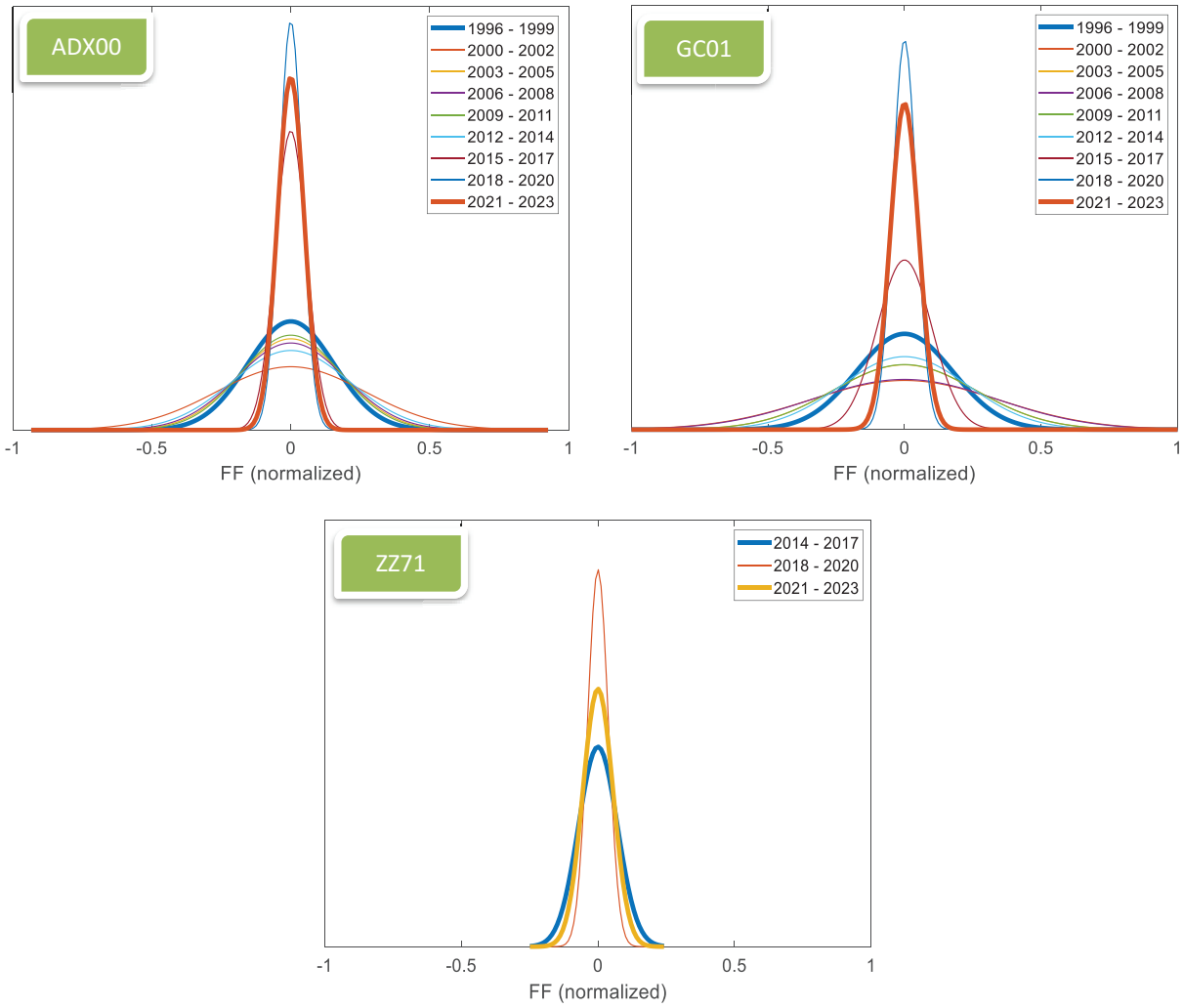

Fig. 5. Gaussian curves modelled and normalized from experimental *FF* data; a similar pattern is observable on all the three plots.

assumes that the same standard deviation would occur for any PV module and hence this standard deviation can be assigned as uncertainty to a single measurement of an otherwise unknown PV module. The coverage factor k determines the probability that a particular interval contains a specific proportion of the distribution: for Gaussian quantities about 68.2% of the data falls within $\pm 1\sigma$ ($k = 1$), 95.4% within $\pm 2\sigma$ and 99.6% within $\pm 3\sigma$ as shown in Figure 4.

In order to deepen the analysis, each module's series has been split into several series each covering a 3-years period, for which the above mentioned process was repeated. Assessing the time evolution of a quantity observed over many years is crucial for understanding how it has changed due to improved technologies. This approach allows a more comprehensive examination of trends, patterns, and factors that contributed to the observed changes. This way the impact of technological advancements on the *FF* determination can be assessed, allowing a better harmonization of methods to tackle future challenges, for example those posed by novel PV materials.

Without losing generality, in the following Figure 5, the entire historical data set of *FF* values from 1996 to 2023 has been divided into shorter timeframes of 3 years each, in order to populate each slot with a sufficient number of samples but at the same time allowing a sufficient resolution to analyze an evolution pattern. For each 3-years period the empirical probability distribution function has been calculated and then fitted with a Gaussian model. Finally, the analytical curves have been normalized (translation to $\mu = 0$ and normalization of the integral value), to be comparable independently on the number of samples for the various periods. The curve of the first and last periods have been highlighted with a bold linewidth to visually evidence the trend, consisting of a reduction of the standard deviation during the years.

Another statistical tool useful for understanding the variability and distribution of data is the IQ (inter-quartile) analysis. A quartile statistical analysis is a method of dividing a dataset into four equal parts, known as quartiles. Quartiles are points that divide a dataset into four equal parts, each containing 25% of the data. The first quartile (Q1) is the median of the lower half of the dataset,

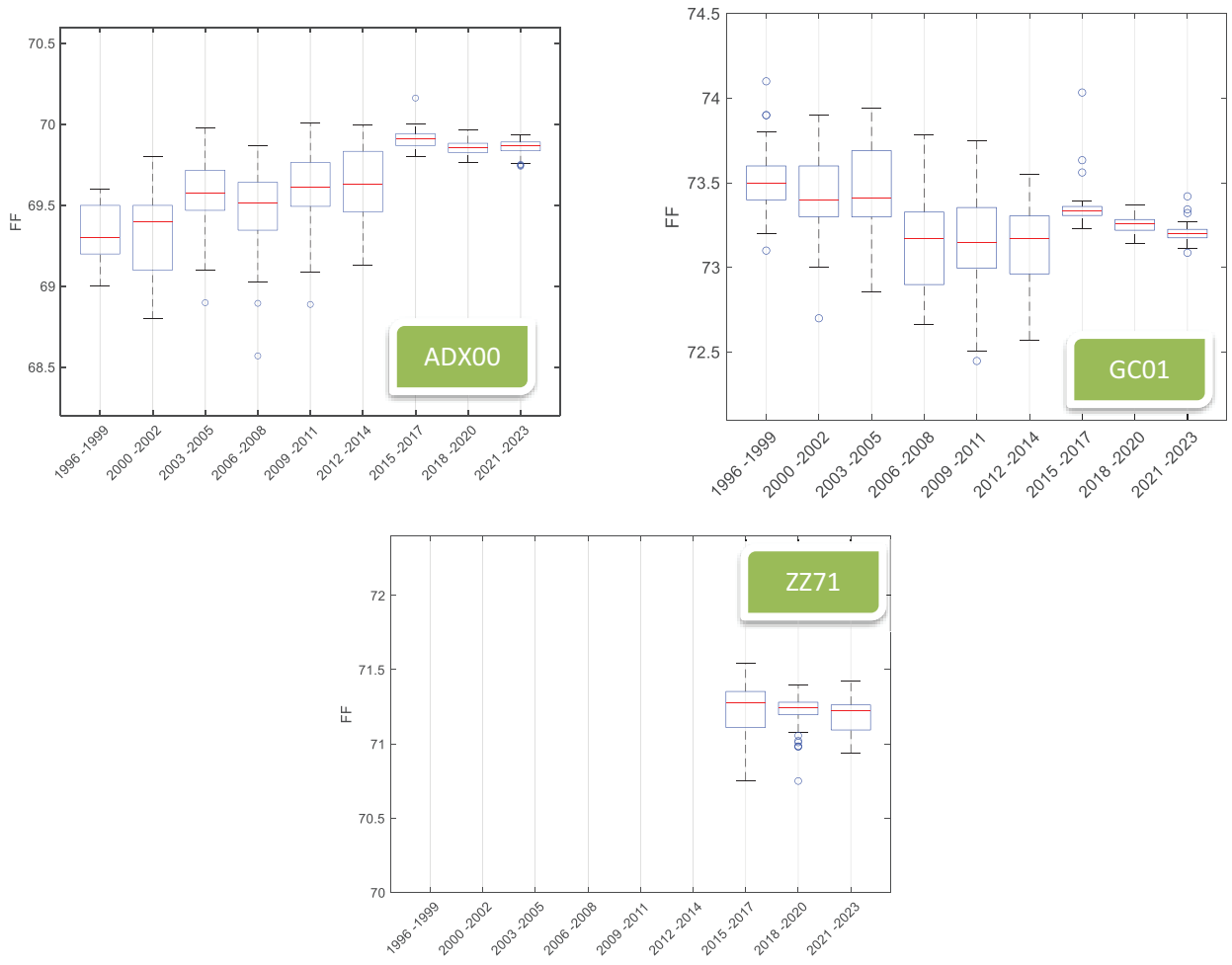

Fig. 6. Box and whiskers plots of the *FF* data sets split into the same periods of 3 years each. The box represents the interquartile range, which is the range containing the middle 50% of the data. It extends from Q1 to Q3. The horizontal line inside the box represents the median (50% percentile). The whiskers extend to the most extreme data points not considered outliers, while the outliers are plotted as points outside the whiskers.

thus the 25% percentile; the second quartile (Q2) is the 50% percentile and so on. The IQ analysis is used in the present study to evidence the outliers and the allocation of the majority of mass of each period's data through box and whiskers plots. The box represents the interquartile range, which is the range containing the middle 50% of the data. It extends from Q1 to Q3. The horizontal line inside the box represents the median (50% percentile). The whiskers extend to the most extreme data points not considered outliers, while the outliers are plotted as points outside the whiskers. Those points that are more than 1.5 times the IQ range away from the bottom or the top of the box are considered outliers.

The box plots of the present data sets are shown in Figure 6. The same time evolution pattern is visible: it is represented by the reduction of the size of the boxes. The average values of the *FF* for each period come from measurements on different solar simulators, and therefore the red lines here do not represent the average values of the repeatability series, due to slight differences between the simulators. There is no relevant change during the years for the median values: ADX00 is basically within the range 69.4 to 69.8, GC01 within 73.2 to 73.5, and ZZ71 in the interval 71.2 to 71.4. However, the amplitude of the boxes and the distance between pair of whiskers in the last periods has appreciably reduced respect to the first years of the analysis, indication of more compact data sets.

Several factors can give possible explanations of this trend: (1) several old generation solar simulators have been replaced by new ones; (2) improvement in the data analysis algorithm for measured I–V curves; (3) improved measurement protocols and better control of ambient conditions in the laboratories.

The majority of the samples of the first periods (before 2013) of ADX00 and GC01 were taken mainly on two simulators with different characteristics: Spectrolab and Pasan2, with major differences in the pulse shape with respect to the other flash source Pasan3B and the steady state Apollo (Fig. 7). Spectrolab had a pulsed forming electronics to stabilize the irradiance, Pasan2 did not have any stabilization process but consisted in the discharge curve of a large array of capacitors injecting power to the Xenon lamp. Pasan3B has a much faster opto-electronic feedback allowing an improved stabilization during the

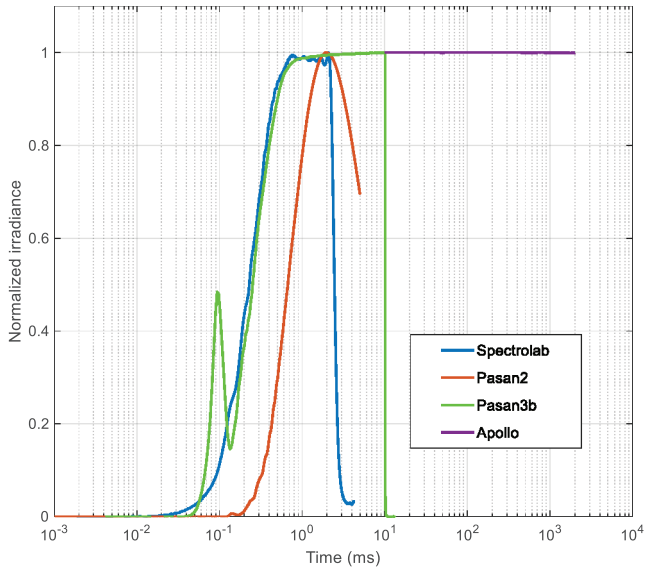

Fig. 7. Normalized shape and duration of the four pulses of the solar simulators on a logarithmic scale. The Apollo does not have a pulse, but a constant irradiance level of the required duration (in the shown case about 1200 ms).

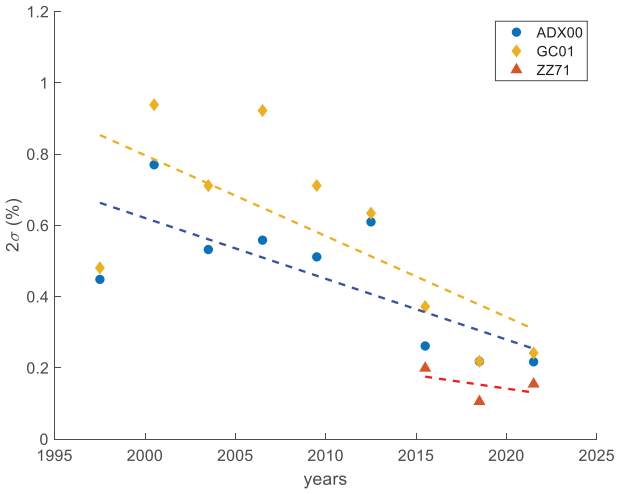

Fig. 8. Evolution of the dispersion of the *FF* values expressed in terms of relative 2σ during the history of measurements.

pulse, and Apollo is a steady state system with typical acquisition lengths of (1–2) seconds. On pulsed simulators, the voltage sweep is triggered by the incoming light at the very beginning of the pulse, then a delay generator adds the required amount of time to skip the rising edge of the flash until the irradiance is stable. On Apollo, the trigger is given via software, because the device is already exposed to light when the measurement starts: an automatized system opens a fast curtain to illuminate the module, and just after it is fully open the voltage sweep is triggered. Although the measured *I*–*V* curves are corrected point-by-point to the desired irradiance (1000 W/m^2 for those of this study with Eqs. (6) and (7)), and the three modules are non-capacitive, a higher quality of the raw data reduces the error due to the correction and therefore minimizes the dispersion of the datasets. The irradiance uniformity has also improved during the years, and simulators of the latest generation are steadily close to values around ±1% on the entire measurement area. The exact impact of the uniformity on the *FF* is not quantifiable using the data in our possession; it depends not only on the irradiance pattern on the module, but also on the cells connections and the position of the limiting cells. Finally, the algorithm used to calculate the $P_{\max}$ value was improved at ESTI. Instead of calculating the $P_{\max}$ from the measured points using simply the largest, a fourth-order polynomial least-square fit is done, considering only an interval of the *I*–*V* curve around the measured $P_{\max}$ point. From the coefficients of the polynomial, the $P_{\max}$ point is analytically calculated imposing zero value to the first derivative. This method allows the calculation of $P_{\max}$ between two consecutive measured points, and as proven to be more robust especially in the case of the Apollo solar simulator, where the number of measured points is lower due to the different data acquisition system respect to the pulsed simulators.

In the latter case, fast digital oscilloscopes are needed to cope with the high speed imposed by the pulse, with acquisitions of 5000 points during the pulse; in the Apollo the data acquisition system is composed by high precision voltmeters acquiring 100 to 300 points during the *I*–*V* measurement. The fitting error for the considered measurements is a minor contribution in the range of ±0.01% to ±0.03% and it is already considered in the statistical analysis. Other improvements have been made on the measurement systems, including reduction in the uncertainty of the internal calibrations of the instruments: temperature sensors, shunts, data acquisition systems are all internally calibrated at ESTI in the framework of the ISO/IEC 17025 accreditation.

Finally, in 2013 the ESTI laboratories moved to a new location, with much better ambient conditions in terms of temperature and humidity, leading to a reduced temperature non-uniformity within the modules under test. An improved temperature control has a direct impact on the uncertainty of $P_{\max}$ and V_{oc}, and therefore on the *FF*.

All the above mentioned results can be better summarized in the following Figure 8.

The blue points represent the 2σ range (twice the standard deviation) of the sample values for each time period and module being considered. These values serve as explicit estimations of the uncertainty contributions, categorized as Type "A" in statistical terminology. They further confirm the trend of reduction of the component attributable to *FF*, as inferred from the slope of the linear least-squares fit (dotted line). The linear fit suggests that at ESTI a revision of the estimation of the *FF* uncertainty component from currently ±0.72% ($k=2$) to values around ±0.3% ($k=2$) might be applicable, leading to a further decrease of the overall uncertainty of $P_{\max}$. This would have a relevant impact on the accuracy of the final results, given that the best-case declared uncertainty for $P_{\max}$ of large area modules at ESTI is already below 1% (±0.95% with $k=2$). The above mentioned result might be applicable to other top-level laboratories, given that the possible causes are in part due to technological

improvements of the equipment, both in terms of optics and electronics. The extension of these results to more recent larger crystalline silicon modules or to other photovoltaic technologies might not be applicable and should be further investigated. However, such a long history of measurements is still not available for devices on the market only for a few years, and the general conclusion that technological improvements on hardware and software of the measurement systems has improved the uncertainty of fill factor is true for all devices.

4 Conclusion

A series of I–V curve measurements taken under the same indoor conditions on three reference modules from 1996 and 2015 have been considered to analyze the FF contribution to the final uncertainty of $P_{\max}$. The FF contribution can be dealt with only as a Type "A" uncertainty, estimated through a series of measured samples. The present work shows through a deep statistical analysis of more than 5200 I–V curves that the uncertainty of FF has decreased during the last decades from ±0.6%–0.7% (k=2) approximately to ±0.3% (k=2). This result is relevant because the FF contribution is a mandatory component for a correct estimation of the $P_{\max}$ uncertainty and has a non-negligible impact on top-level calibration laboratories in the photovoltaic field, whose uncertainties in $P_{\max}$ are already below 1% (k=2). Such a long history of 28 years of measurements indoor is available at ESTI on modules with geometrical characteristics of three decades ago, while it is not yet possible to perform the same analysis on newer devices available on the market. Therefore, the values found in this work might not be directly applicable to them. However, the general conclusion that improvements in the measurement systems and protocols have a positive impact in the reduction of the FF uncertainty is true for every laboratory and all the technologies.

Acknowledgments

The authors would like to acknowledge all the ESTI colleagues past and present who contributed to build this very long measurement series since 1996 and still ongoing.

Funding

The European Solar Test Installation (ESTI) is part of the European Commission Joint Research Centre (JRC). The mission of the Joint Research Centre (JRC) of the European Commission is to provide scientific and technical support to the European Union's policies, strengthening its evidence-based decision-making processes. The JRC focuses on delivering independent, high-quality, and innovative research, as well as fostering collaboration among policymakers, scientists, and stakeholders. The JRC's work spans across various domains, including environment, energy, health, agriculture, industry, and transport, to support the development and implementation of EU policies and contribute to a safer, healthier, and more sustainable future. The JRC is funded by the EU budget.

Conflicts of interest

The authors have nothing to disclose.

Data availability statement

The data used for the present work are part of the measurements performed at ESTI, and not publicly disclosed unless a specific agreement is implemented.

Author contribution statement

Conceptualization, methodology, validation, formal analysis, investigation: D. Pavanello, T. Sample, H. Müllejans; software and data curation: D. Pavanello; Writing – original draft preparation: D. Pavanello; Writing – Review and editing: D. Pavanello, T. Sample, H. Müllejans.

Disclaimer

The views expressed are purely those of the authors and may not in any circumstances be regarded as stating an official position of the European Commission.

References

1. A. Chatzipanagi, A. Jaeger-Waldau, C. Cleret de Langavant, S. Letout, C. Latunussa, A. Mountraki, A. Georgakaki, E. Ince, A. Kuokkanen, D. Shtjefni, *Clean Energy Technology Observatory, Photovoltaics in the European Union – Status report on technology development, trends, value chains and markets – 2022* (Publications Office of the European Union, 2022). https://doi.org/10.2760/812610
2. M. Dada, P. Popoola, Recent advances in solar photovoltaic materials and systems for energy storage applications: a review, Beni-Suef Univ. J. Basic Appl. Sci. **12**, 66 (2023). https://doi.org/10.1186/s43088-023-00405-5
3. T. Bruton, *Photovoltaics from Milliwatts to Gigawatts: Understanding Market and Technology Drivers Toward Terawatts* (John Wiley & Sons, Incorporated, Hoboken, New Jersey, USA, 2021)
4. M.A. Green, E.D. Dunlop, M. Yoshita et al., Solar cell efficiency tables (Version 63), Prog. Photovolt.; Res. Appl. **32**, 3 (2024). https://doi.org/10.1002/pip.3750
5. IEC60904-9: 2020. Photovoltaic Devices – Part 9: Classification of solar simulator characteristics (2020). https://webstore.iec.ch
6. IEC60904-1: 2020. Photovoltaic devices – Part 1: Measurement of photovoltaic current-voltage characteristics (2020). https://webstore.iec.ch
7. IEC61853-1: 2011. Photovoltaic (PV) module performance testing and energy rating – Part 1: Irradiance and temperature performance measurements and power rating (2011). https://webstore.iec.ch
8. IEC60904-3: 2019. Photovoltaic devices – Part 3: Measurement principles for terrestrial photovoltaic (PV) solar devices with reference spectral irradiance data (2019). https://webstore.iec.ch

9. BIPM, IEC, IFCC, ILAC, ISO, IUPAC, IUPAP, and OIML. Evaluation of measurement data — Guide to the expression of uncertainty in measurement. Joint Committee for Guides in Metrology, JCGM 100: 2008 (2008). https://www.bipm.org
10. IEC60891: 2021. Photovoltaic devices – Procedures for temperature and irradiance corrections to measured *I–V* characteristics (2021). https://webstore.iec.ch
11. D. Pavanello, R. Galleano, W. Zaaiman, M. Ankit, N. Kouremeti, J. Gröbner, K. Hoogendijk, M. Po, E.F. Lisbona, W. Alius, D. Dosenicova, I. Kroeger, D. Friedrich, E. Haverkamp, A. Minuto, E. Celi, M. Pravettoni, G. Bellenda, R. Fucci, Results of the IX International Spectroradiometer Intercomparison and impact on precise measurements of new photovoltaic technologies, Prog. Photovolt.: Res. Appl. **29**, 109 (2020). https://doi.org/10.1002/pip.3347
12. J.M. Gee et al., Contact resistance and fill factor in silicon solar cells, IEEE Trans. Electron Dev. **35**, 2086 (1988)
13. A. Shah et al., Fill factor losses due to contact resistance in thin-film solar cells, J. Appl. Phys. **86**, 6296 (1999)
14. J. Chen et al., Influence of contacting parameters on fill factor in PERC solar cells, J. Electrochem. Soc. **165**, G115 (2018)
15. M. Pravettoni, D. Poh, J. Prakash Singh, J. Wei Ho, K. Nakayashiki, The effect of capacitance on high-efficiency photovoltaic modules: a review of testing methods and related uncertainties, J. Phys. D: Appl. Phys. **54**, 193001 (2021). https://doi.org/10.1088/1361-6463/abe574

Cite this article as: Diego Pavanello, Tony Sample, Harald Müllejans, An investigation on the uncertainty of fill factor, EPJ Photovolt. **16**, 2 (2025)